Experimental perspective on the mechanisms for near-wall accumulation of platelet-size particles in pressure-driven red blood cell suspension flows

Gonçalo Coutinho [*]
IN+ Center for Innovation, Technology and Policy Research, Instituto Superior Técnico, University of Lisbon, Portugal

Ana S. Moita
IN+ Center for Innovation, Technology and Policy Research, Instituto Superior Técnico, University of Lisbon, Portugal
and CINAMIL–Military Academy Research Center, Militart Academy, Portugal

Massimiliano Rossi
Department of Industrial Engineering, Alma Mater Studiorum University of Bologna, Italy
and Department of Physics, Technical University of Denmark, Denmark

António L. N. Moreira
IN+ Center for Innovation, Technology and Policy Research, Instituto Superior Técnico, University of Lisbon, Portugal

(Received 19 January 2023; accepted 13 September 2023; published 2 October 2023)

The root causes for the mechanisms for margination and near-wall platelet accumulation have previously been investigated by numerical simulations and the results pointed to two main contributors. First, the behavior of the red blood cells (RBCs), namely, traveling around the centerline and formation of the cell-free layer (CFL). Second, the multiple interactions between RBCs and platelets. However, these mechanisms remain to be experimentally verified. In this work, we focus on the dynamics of platelet-size particles inside RBC flows through straight-square microchannels. We used rigid particles with nominal diameter of 2.47 μm to mimic platelets. The three-dimensional (3D) coordinates (x, y, z) and velocity components (v_x, v_y, v_z) of the platelet-size particles inside the RBC-suspension flows were measured by means of the general defocusing particle tracking method (GDPT). From the 3D particle trajectories, we were able to investigate the root causes for margination and near-wall particle accumulation. The overall picture points to the RBCs as the dictator of the near-wall particle accumulation and margination. We show that the phenomenon of margination is an irreversible, fast, unpredictable and discontinuous process, and more importantly it can be an opportunity-based event.

DOI: 10.1103/PhysRevFluids.8.103101

I. INTRODUCTION

Near-wall circulation of platelets in microvascular flows plays an important role in the formation of hemostatic plug [1] and thrombus [2]. In vascular flows, it is well-known that healthy red blood cells (RBCs) travel preferably around the center-line of the vessel (RBC-rich region) [3,4], creating

[*]goncalo.coutinho@tecnico.ulisboa.pt

 ©2023 American Physical Society

a RBC-depleted region near the wall known as cell-free layer (CFL) [5,6]. Platelets, however, will be forced to travel inside the CFL due to the multiple interactions with RBCs [7–9]. In other words, platelets in vascular flows migrate from the core of the RBCs toward the CFL. The phenomenon that describes this migration of platelets in vascular flows is referred to as "margination." The margination and near-wall circulation is not limited to platelets, and in fact extends to other rigid particles flowing in blood vessels such as white blood cells [6] or even synthetic particles [10]. The latter are known to be a promising technology for drug delivery scenarios [11]. By flowing close to the vessel wall, rigid particles promote the drug delivery to the endothelial cells. Another perspective over rigid particles in vascular flows concerns unhealthy RBCs. Under certain pathological conditions, unhealthy RBCs loose the deformability, i.e., the membrane becomes more stiff as in malaria-infected RBCs [12,13] or in type 2 diabetes mellitus RBCs [14,15]. In such conditions, the unhealthy RBCs behave as the other rigid particles in vascular flows and marginate.

The phenomenon of margination was first observed in 1980 by Schmid-Schönbein *et al.* [16] with *in vivo* experiments and since then it has drawn significant attention due to the physiological relevance. Throughout the years, several numerical simulations [17–24] and experimental studies [25–30] have been dedicated to the subject. The majority of the experimental studies have focused on the conditions that lead to higher margination propensity. For instance, by adjusting the particle diameter [27,29], shear rate [23], shape of the particle [26], hematocrit (Hct) [25] and even the geometry of the microchannel [24,28]. Although these studies contribute to the development of new drug carrying particles and blood-based medical devices, as yet in general they have not examined the mechanisms that actually lead to margination and to near-wall particle accumulation.

Two mechanisms are pointed as the root cause for margination and the near-wall platelet accumulation. On the one hand, we have the wall-induced lift force propelling the deformable RBCs away from the wall and leading to the formation of the CFL [31–33]. The absence of RBCs inside the CFL results in lack of platelet-RBC collisions and hence in low platelet diffusivity in the region [19]. Under low collision frequency, platelets lack of an ejecting mechanism that would enable the migration back to the RBC-rich region. On the other hand, we have the inevitable collisions between platelets and RBCs inside the RBC-rich region that lead to the migration of platelets toward the CFL, i.e., margination. It has been shown that in collisions between stiff and floppy particles, the stiffer particle undergoes a larger displacement [22,34].

Over the last decade, several numerical investigations [17–21] have focused on developing models to predict platelet margination in blood flows. Crowl and Fogelson [17] used Lattice-Boltzmann method to model whole blood dynamics, with the results showing a nonuniform platelet diffusion in the lateral direction. With direct numerical simulations of RBCs and platelets suspensions, Mehrabadi *et al.* [19] reported the platelet margination as an irreversible process. Using the a three-dimensional (3D) computational model Vahidkhah *et al.* [18] studied the dynamics of platelets in whole blood. The authors also reported the margination process as irreversible. Similar conclusions were drawn by the theoretical model of Qi and Shaqfeh [20]. More recently, Závodszky *et al.* [21] used cellular blood flow simulations to study RBC and platelet diffusivity. The authors also showed a nonuniform platelet diffusivity along the lateral direction, and in addition they determined a platelet lateral drift toward the wall.

On the experimental side, previous authors used platelet-size particles to mimic platelets, however to evaluate the platelet-size particle distribution within RBC-suspension flows. For instance, we have the early examples of Tilles and Eckstein [8] and Eckstein *et al.* [35], and more recently the particle tracking velocimetry (PTV) measurements of Carboni *et al.* [27] where fluorescent polystyrene (PS) particles where added to RBC suspensions. Yet none of these studies was able to look into the root causes as reported by the aforementioned numerical simulations. Evidently, the experimental characterization of the dynamics of platelet-size particles in blood flows is often difficult. First, the RBCs mask the particles and detection becomes challenging [27], and second particle-RBC interactions are expected to have a 3D nature [18] and the classical PTV method is limited to two dimensions. Up to now, to the author's best knowledge, the root causes pointed by

the numerical simulations for the margination and near-wall platelet accumulation remain to be experimentally verified.

To provide experimental evidence on the mechanisms that lead to margination and near-wall platelet accumulation, in this work we focus on the dynamics of platelet-size particles inside RBC-suspension flows through straight microchannels with square cross-sectional area. We used rigid-fluorescent PS microspheres with nominal diameter of 2.47 μm to mimic platelets. To obtain a 3D characterization of the platelet-size particles dynamics inside the RBCs flow, we use a single-camera 3D PTV method, referred to as general defocusing particle tracking (GDPT) [36–38], to obtain the 3D coordinates (x, y, z) and velocity components (v_x, v_y, v_z) of the platelet-size particles inside the RBC-suspension flows.

First, the GDPT method is introduced in Sec. II B 1, and the flow is characterized by means of the velocity profiles and viscosity of the RBC suspensions in Sec. III A. The particle dynamics and distribution inside the RBC-suspension flows is studied in Sec. III B. We start by evaluating the individual particle trajectories obtained with GDPT method, and subsequently we perform a quantitative analysis based on the particle diffusivity, drift velocity and distribution along the two crossflow directions (y and z). The results on phenomenon of margination are given in Sec. III C, where we correlate the particle dynamics with the trajectory of particles flowing close to the CFL. Based on our results, we discuss the root causes for margination and near-wall particle accumulation in Sec. IV, while providing a comparison with previous studies.

II. EXPERIMENTAL METHODS

A. Sample preparation

A solution of bovine washed RBCs at Hct = 100 % (IBORBC100P, Innovative Research, Co., USA) was used to prepare the RBC suspensions. The initial solution of RBCs was diluted in phosphate-buffered saline (PBS) (×1.0, ph = 7.4, FisherScientific, Co., USA) to obtain the desired hematocrit levels (Hct = 10, 15, 20, 25, 30 %) and platelet-size fluorescent PS microspheres with nominal diameter of 2.47 μm (530/607 nm, PS-FluoRed, MicroParticles GmbH, Germany) were added to each sample [27]. The selected range of hematocrit corresponds to the value inside the inlet reservoir, also known as feed hematocrit. Please note that in our experiments, the hematocrit inside the microchannel (i.e., tube hematocrit) is expected to be smaller than the reservoir hematocrit as consequence of the Fahreus-Lindqvist effect [39], and that henceforth, Hct will always refer to the reservoir hematocrit. A single solution was prepared for each Hct.

B. Experimental setup

Figure 1 shows the schematic of the experimental setup and measurement principle. All measurements were performed in a single microchannel featuring a square cross-section ($w_{ch} \times h_{ch} = 50 \times 50\ \mu m^2$) and a total length L_{ch} of 58.5 mm (CS-10000087, Darwin Microfluidics, France). The microchannel was made of a rigid polymer (Topas COC) and it was supported with an additional 1-mm-thick glass microscope slide (D100001, Deltalab, Spain), see Fig. 1(b).

The RBC suspensions were driven through platinum-cured silicone tubing (SHE-TUB-SIL, Darwin Microfluidics, France) from an inlet reservoir to the microchannel, using hydrostatic pressure. The hydrostatic pressure was imposed by setting an offset (h_p) between the inlet and the collection reservoir using a millimeter stage (Edmund Optics Co., USA). The reference Poiseuille flow for a PBS solution, i.e., in the absence of RBCs, corresponds to a flow rate of $Q_p = 0.22$ μl/min and a mean velocity of $\bar{v}_x = 1.4$ mm/s. The wall-shear rate was estimated according to the work of Son [40] and it yielded $\dot{\gamma} = 228\ s^{-1}$. To ensure the reproducibility of the flow, the data were acquired twice per hematocrit. Between measurements the whole system was flushed and the microchannel rinsed with distilled water for 10 minutes. Additionally, the RBC suspensions were gently agitated before the measurements to minimize sedimentation.

The imaging system consisted of an epi-fluorescent inverted microscope (DM IL LED, Leica GmbH, Germany) equipped with a high-speed camera (HighSpeedStar 4G, LaVision GmbH,

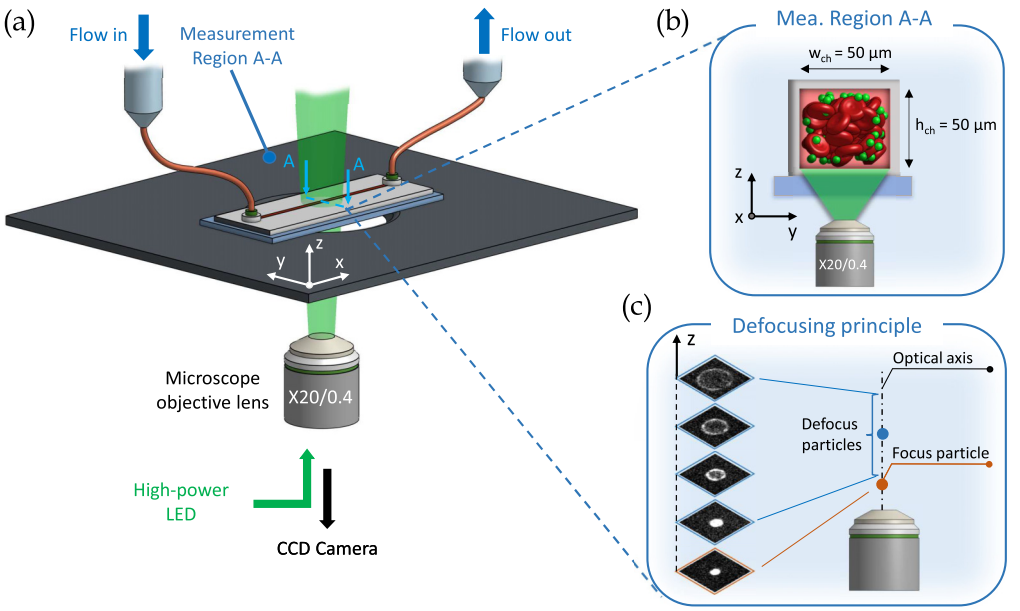

FIG. 1. Schematic of the experimental setup and measurement principle. (a) Schematic of the GDPT experimental setup used for the tracking of the platelet-size particles inside the RBC-suspension flows. (b) Schematic of the measurement region. (c) Defocus principle used for defocus particle tracking methods such as GDPT.

Germany). The system was operated with a 20 × /0.4 objective lens (NPlan Epi, Leica GmbH, Germany) which yielded a spatial resolution of 0.85 µm/pixel. The field was illuminated using a high-power green LED (SolisC525C, Thorlabs Inc., USA) and a filter cube for fluorescence imaging (Excitation:BP 525/50 nm; Dichroic: 570 nm and Emission: 620/60 nm).

1. Defocusing particle tracking of the platelet-size particles

The 3D coordinates (x, y, z) and velocity components (v_x, v_y, v_z) of the platelet-size particles inside the RBC-suspension flows were obtained using a single-camera 3D PTV method known as GDPT [37,38]. The fluorescent particles exhibit unique defocused particle images depending on their position along the optical axis, i.e., their depth position; see Fig. 1(c). Under these conditions, the 3D positions of the particles are recovered using a suitable mapping of the defocused particle images for the depth coordinate (z), and the in-plane coordinates (x, y) are obtained from the center of the particle images. The mapping consists of a calibration image stack which is obtained by taking images of a platelet-size particle sedimented on the bottom of the microchannel and adjusting the depth position by moving the objective lens. In our measurements, the calibration stack was obtained by adjusting the focus position of the objective lens at constant steps of 1 micron. We obtained a measurement depth h of 100 µm with our optical configuration, thus the entire volume could be observed with a single measurement. For further reading on the GDPT method the reader should refer to Barnkob and Rossi [37].

All measurements were performed near the end of the microchannel ($\Delta x = 45$ mm; $\Delta x/L_{\text{ch}} \approx 76\,\%$) to ensure that most of the particles have already marginated. The flow was recorded using a total of 2500 dark-field images of the fluorescent platelet-size particles, acquired at a frame rate of 50 Hz. The recorded dark-field images were processed using the DefocusTracker software [41]. Briefly, the particle detection and coordinates estimation is performed by matching experimental and

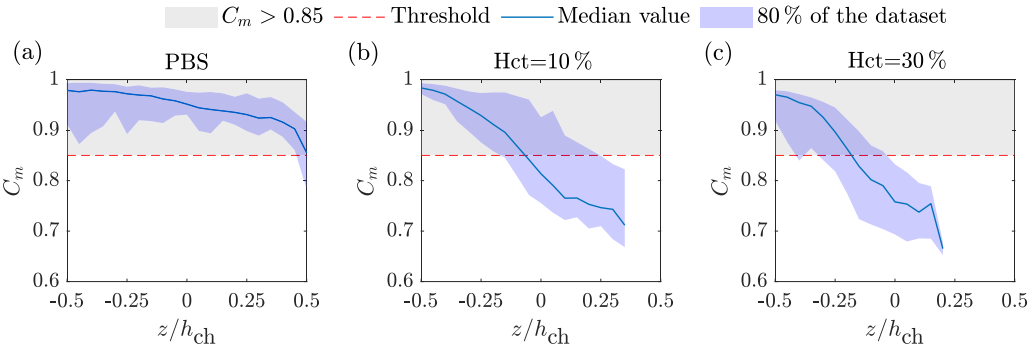

FIG. 2. Distribution of the similarity C_m between calibration and experimental images obtained from the GDPT evaluations, as function of the depth coordinate z, including the median value and a 80 % distribution of the dataset. (a) PBS solution (absence of RBCs). (b) Hct = 10 %. (c) Hct = 30 %.

calibration images with normalized cross-correlation [42]. Since the particle density was low, the particle tracking was performed with the nearest-neighbor algorithm [43]. The software is available at Ref. [44]. Additionally, as postprocessing step we used a mean-based outlier detection to remove spurious velocity vectors from the GDPT evaluation: Velocity vectors with more than three standard deviations from the mean value in the neighborhood were removed. Overall, the outliers represented less than 2 % of the dataset for all measurements.

In this type of measurements, the particle coordinates estimated with the GDPT method are biased due to the presence of the field curvature aberration [38,45]. To correct this bias, we used a procedure based on a reference measurement of a Poiseuille flow as described in Coutinho *et al.* [46]. Here, the correction was obtained by using the trajectories of the platelet-size particles, see also Coutinho *et al.* [47]. It should be noted that without correction the magnitude of this bias error was up to 3.4 % of the measurement depth h.

The measurement uncertainty was estimated using a reference measurement of a Poiseuille flow in the absence of RBCs, as in Barnkob and Rossi [37]. In particular, we used the displacements in y and z direction, considering null-displacement as the true value. We obtained the following uncertainties $\sigma_{x,y} = 0.55$ μm and $\sigma_z = 1$ μm. Besides, it was noted that the RBCs flowing inside the microchannel mask the defocused images of the tracer particles, hence degrading the determination of the depth coordinate z. In turn, this has no contribution to the determined in-plane coordinates x and y, since they are obtained from the center of the particle image. To evaluate its impact on the GDPT evaluation, we can compare the degree of similarity between the calibration and experimental images given by the maximum value of the normalized cross-correlation, C_m [38], a parameter that varies between 0 and 1, where 1 to corresponds to a perfect match between a calibration and an experimental defocused particle image. Figure 2 shows the similarity C_m as function of the depth coordinate z for the PBS solution (in the absence of RBCs), and Hct = 10, 30 %, including the median value and a 80 % distribution of the dataset. Again, please note that the impact of the RBC masking will only be determinant for the depth coordinate z, as it will depend on the number of flowing RBCs that are positioned between the tracer particle and the objective lens.

The results shown in Figs. 2(a) to 2(c) highlight the degradation on the particle detection as function of the depth coordinate. Whereas for the PBS solution the majority of the data-points lie above 0.9, in the presence of the RBCs the datapoints show a larger dispersion in C_m. Furthermore, it is also shown that in the RBCs flow, the particle detection is not possible above a limit depth. Following the present results, we defined a threshold for C_m at 0.85 and excluded the data from points below, as illustrated in Fig. 2. As a consequence, the determined vertical coordinate will be then constraint to $-0.5 < z/h_{ch} < -0.15$ throughout the present work.

2. Cell-free layer visualization

To characterize the CFL, we recorded bright-field images of the RBCs flow. The CFL was then determined by post-processing each recorded frame using threshold-based image processing methods to determine the boundary of RBC-rich region across the length of the FOV, as well as the position of the wall of the microchannel. Here, the thickness of the CFL (δ_{CFL}) was calculated by finding the distance between boundary of the RBC-rich region and the wall. The values were averaged in space for each frame and the final value represents an mean value from all recorded frames. Please note that since our optical setup only allows to observe the microchannel through the bottom wall, we assume that the CFL determined for the y axis is also valid for the z axis. Such assumption derives from the symmetry of the microchannel's cross section.

C. Velocity profile

The velocity distribution $v_x(y, z)$ of the platelet-size particles was extracted from the 3D particle trajectories provided by the GDPT measurements. For comparison, we projected the velocity distribution along the spanwise y and vertical z directions, and the velocity profiles were fitted to an empirical equation derived from the solution for Poiseuille flow velocity in straight-square microchannels,

$$v_x = v\left(\frac{\cosh(0.5^m) - \cosh(|y^*|^m)}{\cosh(0.5^m) - 1}\right) + v_0, \tag{1}$$

where v and v_0 are the fitting parameters based on the velocity distribution (v_x), and m is a fitting parameter based on the velocity profile bluntness (see, e.g., Passos *et al.* [30]). Here, the coordinate y^* is normalized with the width w_{ch} of the microchannel. The same expression is valid for the vertical direction z, with the coordinate being normalized with the height h_{ch} of the microchannel.

D. Viscosity of RBC suspensions

The viscosity of RBC suspensions is known to vary with hematocrit and to have influence on the shape of the velocity profiles [25]. To compare, we estimated the relative viscosity for the different RBC-suspension flows. Due to the non-Newtonian behavior of blood, the viscosity of the RBC suspensions is expressed as an apparent viscosity μ_{app} [48–50] using the analytical solution of a Poiseuille flow in a microchannel with square cross-section and it is given by

$$\mu_{\mathrm{app}} = \frac{h_{\mathrm{ch}}^3 w_{\mathrm{ch}} \Delta P}{12QL}\left[1 - \sum_{n,\mathrm{odd}}^{\infty} \frac{1}{n^5}\frac{192}{\pi^5}\frac{h_{\mathrm{ch}}}{w_{\mathrm{ch}}}\tanh\left(n\pi\frac{w_{\mathrm{ch}}}{2h_{\mathrm{ch}}}\right)\right], \tag{2}$$

where h_{ch} and w_{ch} are the height and width of microchannel, respectively, $\Delta P/L$ the imposed pressure gradient and Q the volumetric flow rate [51]. The relative viscosity μ_{rel} is obtained by comparing the apparent viscosity with and without flowing RBCs. For the latter, we used a PBS solution as working fluid. The mathematical expression is as follows:

$$\mu_{\mathrm{rel}} = \frac{\mu_{\mathrm{app}}}{\mu_{\mathrm{PBS}}} = \frac{Q_{\mathrm{PBS}}}{Q_{\mathrm{RBC}}}, \tag{3}$$

where Q_{RBC} and Q_{PBS} represent the flow rate with and without flowing RBCs, respectively. To compare the present experiments with previous studies, the relative viscosity was subsequently analysed using the empirical model given by Pries *et al.* [52],

$$\mu_{\mathrm{rel}} = 1 + B[(1 - \mathrm{Hct})^C - 1], \tag{4}$$

where B and C are fitting parameters and Hct is the hematocrit at the inlet reservoir (i.e., feed hematocrit). For our measurements, we used the fitting parameters B and C provided by Pries *et al.* [52] ($B = 3.54$; $C = -0.743$). which were obtained from the measurements of Bayliss [53] in a microchannel with a tube diameter of $D = 55\,\mu$m. We selected these values based on the available data, as they closely resembled the conditions of the current experiments.

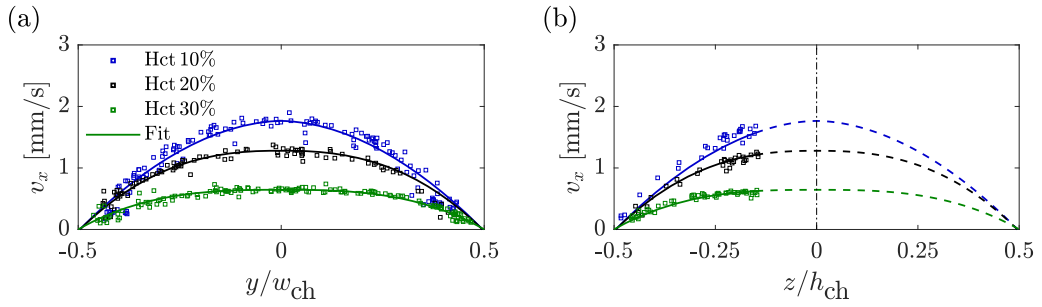

FIG. 3. Velocity profiles v_x of the platelet-size particles in RBC-suspension flows at Hct = 10, 20, 30 %. (a) Spanwise direction y. (b) Vertical direction z ($-0.5 < z/h_{ch} < -0.15$). Reproduced from Coutinho *et al.* [46].

III. RESULTS

A. Flow characterization

Figures 3(a) and 3(b) show the velocity profiles of the platelet-size particles in the RBC-suspension flows at different hematocrit levels (Hct = 10, 20, 30 %). The velocity data was fitted using Eq. (1), and the particle coordinates, y and z, were normalized according to the dimensions of the microchannel cross-section w_{ch} and h_{ch}, respectively (Sec. II C). At low hematocrit (Hct = 10 %), the velocity profile resembles the distribution of a Newtonian fluid [51]. However, at larger RBC concentrations (Hct = 20, 30 %), the velocity distribution exhibits a blunter profile. This blunter profile is consistent with previous *in vitro* studies [27,54,55] and arises most likely due to both the formation of the CFL and the larger number of RBCs flowing around the centerline of the microchannel. Following the present flow characterization, we also evaluated the particle sedimentation across our FOV for a PBS solution (i.e., in the absence of RBCs). We determined, for each individual track, the variation of the particle vertical coordinate z (ΔZ) so that: $\Delta Z = z(N) - z(1)$, where $z(1)$ is the first particle position and $z(N)$ is the last particle position for a given track. Here, ΔZ is a measure of the particle decay, i.e., sedimentation, across our FOV. In our experiments, we computed the median value of ΔZ which yielded in the order of $O(10^{-4})$, from which we concluded that we do not have significant particle sedimentation in our experiments.

The velocity distributions also exhibit a decrease in the maximum velocity as function of increasing Hct; see, e.g., Fig. 3(a). It is well-established that the viscosity of RBC suspensions increases with hematocrit [56–58]. For flow conditions imposed by a constant pressure drop, as in our measurements, larger pressure drops are required to drive the flow at the same velocity for higher Hct. This observation is confirmed by the estimated relative viscosity μ_{rel} shown in Fig. 4. Moreover, the estimated values μ_{rel} show a good correlation with the empirical model given by Pries *et al.* [52]. It is worth noting that the relative viscosity provides a measure of the overall behavior of the RBC suspensions, however in fact the local viscosity has an heterogeneous distribution in this type of flows [59]. Since there are more RBCs flowing around the center of the microchannel, we expect larger viscosity in the middlemost region of flow, whilst taking lower values within the RBC-depleted region, i.e., inside the CFL.

Another important topic regarding the flow characterization is the RBCs sedimentation. Although we did not investigate the RBCs sedimentation alone, we believe that such effect has a small contribution to our experiments for the following reasons. First, in the presence of RBCs sedimentation, there would be more RBCs flowing close to the bottom of the channel, hence increasing the local viscosity. As a consequence, we would expect a variation of the local velocity on the lower part of the channel. By comparing the velocity profiles from Figs. 3(a) and 3(b), we see that the velocity profiles (v_y and v_z) are similar. Second, as shown by Alonso *et al.* [60], for this type of flows, mainly the upper part of the channel is RBC deficient. However, due to the RBC-induced masking (Sec. II B 1)

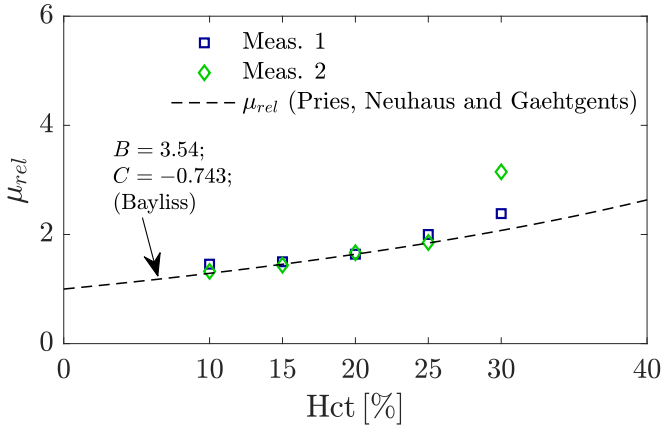

FIG. 4. Estimated relative viscosity μ_{rel} as function of hematocrit (Hct) (e.g., Pries *et al.* [52]), with the values *B* and *C* corresponding to the experiments of Bayliss [53]. The different markers refer to results from two different measurements (Meas. 1, Meas. 2) for the same flow conditions.

this region was excluded from our measurements. Accordingly, the effect of RBC sedimentation is expected to be small in our experiments.

B. Particle dynamics and distribution inside the RBC flow

To characterize the dynamics of the platelet-size particles inside the RBC-suspension flows, we first selected individual particle trajectories from the GDPT evaluation. For comparison, we considered trajectories of particles flowing inside the RBC-rich region, as well as inside the CFL which is here represented by the gray-shaded area. Figure 5 shows the sample particle trajectories for Hct = 10 % and Hct = 30 %.

In general, the particles flowing inside the RBC-rich region exhibit large displacements along the spanwise and vertical directions, as shown in Fig. 5. Since this is a pressure-driven flow, inside

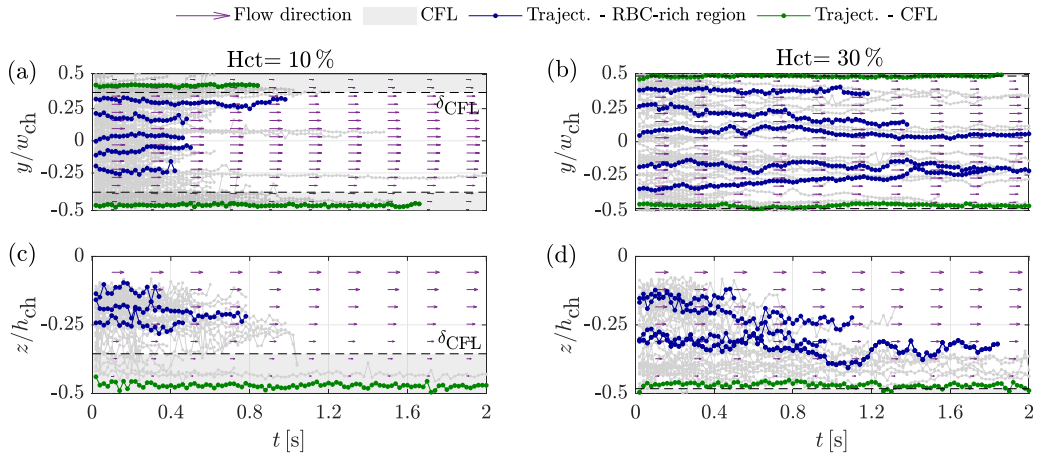

FIG. 5. Sample trajectories of platelet-size particles within RBC-suspension flows at Hct. 10 % and Hct. 30 % including the trajectories inside the RBC-rich region and inside the CFL. (a), (b) Spanwise direction *y*. (c), (d) Vertical direction *z*. The flow direction is shown by the arrows (→), the CFL is represented by the gray-shaded area (■) and δ_{CFL} represents the thickness of the CFL. Adapted from Coutinho *et al.* [46].

a straight microchannel with constant cross-sectional area and no external forces are applied to the system, such displacements arise from the continuous, random collisions with the RBCs [18,51]. Please note that in collisions between stiff and floppy particles, the stiffer particle undergoes a larger displacement [22,34]. However, inside the CFL, the particles exhibit trajectories almost parallel to the wall of the microchannel, with only minor displacements along the the spanwise y and vertical z directions; see, e.g., Figs. 5(a) and 5(b). Here, the particles are confined between the RBCs flowing at the boundary of the RBC-rich region and the wall of the microchannel. Since there are no flowing RBCs inside the CFL, the collisions are only promoted at boundary of the RBC-rich region and the magnitude of the fluctuations in the particle trajectories decreases [18].

Following the qualitatively analysis on the particle dynamics from the sample trajectories shown in Fig. 5, throughout the present section we will present a quantitatively analysis of the particle dynamics and distribution inside the RBC-suspension flows. First, the particle diffusivity is discussed in Sec. III B 1. The particle drift velocity is presented in Sec. III B 2, and ultimately the particle concentration distribution is addressed in Sec. III B 3.

1. Particle diffusion

The particle diffusivity (D_i) was estimated from the individual particle trajectories. Assuming that the particle motion in RBC-suspension flows is a standard diffusion process, the particle diffusivity can be computed from the mean square displacements as function of time according to

$$D_y = \frac{1}{N}\sum_{i=1}^{N}\frac{[y_i(t_0+\Delta t)-y_i(t_0)]^2}{2\Delta t}, \tag{5}$$

where y represents the particle coordinate (also valid for z), t_0 the reference time and Δt the time interval between consecutive image frames (20 ms) and N the number of tracked particles [19,61]. The selected time window Δt corresponds to the camera recording frequency and enables to capture several collision events [21]. The values are averaged in space along the mean flow direction x. For the calculations of D_y, we divided the width of the microchannel into n bins equally spaced and with width approximately equal to the particle diameter ($\approx$2.5 μm). For the z coordinate, the same procedure was applied but along the height of the microchannel. To ensure statistical significance, we only considered the bins including more than 50 datapoints. Please note that the contribution from the Brownian motion to the particle diffusivity to the shear-induced diffusivity is typically neglected [17,21]. To have a measure of the Brownian diffusivity, we calculated the particle diffusivity for the PBS solution (i.e., in the absence of RBCs) ($D_y = 0.15 \times 10^{-7}$ cm^2 s^{-1}) which yielded an order of magnitude lower than the RBC-induced diffusivity, as we will show throughout this Section. Similar results were obtained in the experiments of Carboni *et al.* [27]. For comparison, the results obtained for the PBS solution and different hematocrit (Hct = 15, 25, 30 %) are shown in Figs. 6(a)–6(d) for the spanwise direction y, and in Figs. 6(e)–6(h) for the vertical direction z. Please note that the vertical coordinate was limited to $-0.5 < z/h_{ch} < -0.15$ due to the masking effects of the RBCs, as discussed in Sec. II B 1. Similar results were obtained for the remaining hematocrit.

The mean value of the particle diffusivity along the spanwise direction y at Hct = 30 % yielded $D_y = 1.02 \times 10^{-7}$ cm^2 s^{-1}, which is in the same order of magnitude as those reported in experiments of Carboni *et al.* [27] and in the numerical simulations of Crowl and Fogelson [17] at low shear rate ($\dot{\gamma} = 400\,\text{s}^{-1}$). In addition, the present value shows good agreement with the experiments of Turitto *et al.* [62], where the platelet diffusion in whole blood was also measured at low shear rates [$D_y \sim \mathcal{O}(10^{-7})$]. Závodszky *et al.* [21] reported values one order of magnitude larger, however their numerical simulations were conducted at higher shear rates, thus the diffusivity is expected to be larger, as shown by Crowl and Fogelson [17].

Concerning the distributions, the presence of the RBCs originates a nonuniform lateral and vertical profile in the particle diffusivity; see, e.g., Figs. 6(b)–6(d). A large particle diffusivity is

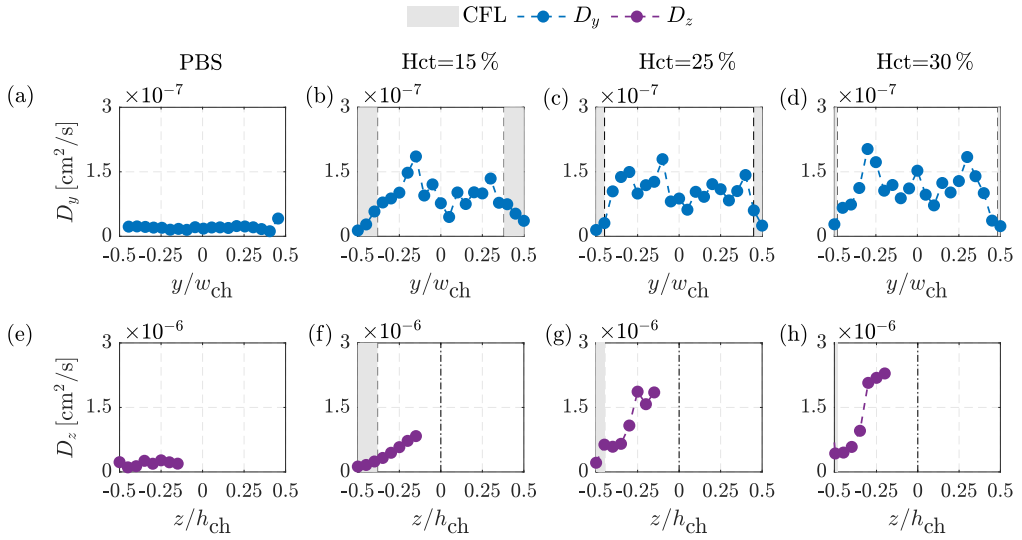

FIG. 6. Diffusivity distribution of the of the platelet-size particles D_{d_y} along the crossflow directions y and z for the PBS solution and different RBC concentrations: Hct = 15, 25, 30 %. (a)–(d) Distribution D_y along the spanwise direction y. (e)–(h) Distribution D_z along the vertical direction z ($-0.5 < z/h_{\mathrm{ch}} < -0.15$). The CFL is represented by the gray-shaded area (■).

found inside the RBC-rich region: A consequence of the continuous, random collisions with the RBCs. Approaching the CFL, there is a steep decrease in particle diffusivity toward the wall of the microchannel. A similar behavior was reported in the simulations of Crowl and Fogelson [17] and Závodszky *et al.* [21]. This steep gradient is attributed to the decrease in the number of RBCs as one approaches the CFL [19], which will accordingly gradually reduce the number of particle-RBC collisions, hence the particle diffusivity decreases. Without surprise, the minimum values in the particle diffusivity are found within the CFL. As observed from the sample particle trajectories, such behavior arises due to the absence of RBCs inside the CFL. In the end, the RBCs dictate the particle diffusivity as reported in previous works; see, e.g., Vahidkhah *et al.* [18]. Another supporting argument arises from the comparison of the particle diffusivity for PBS solution and those with RBCs. Whereas for the latter we estimated a nonuniform distribution, the former exhibited a rather uniform distribution while in addition showing a particle diffusivity an order of magnitude lower.

Comparing the two crossflow directions y and z, we observe a similar steep gradient in the particle diffusivity when approaching the CFL, which is sited around the same location. However, the diffusivity along the vertical direction z, although comparable to the y direction, is found to be larger. These larger values are most likely a measurement artifact due to the increased uncertainty of the GDPT evaluation in the depth direction. As discussed in Sec. II B 1, the particle detection degraded due to the masking-effect of the RBCs, and this effect increases as the hematocrit is increased. Accordingly, it is expected that the uncertainty in determining the z position becomes larger, which will also translate in more position fluctuations, hence bias the particle diffusivity along the vertical direction. We will return to this point in Sec. III B 2.

2. Particle drift velocity

The drift velocity of the platelet-size particles (v_y and v_z) was extracted from the individual particle trajectories using the following equation

$$v_y = \frac{1}{N}\sum_{i=1}^{N}\frac{[y_i(t_o+\Delta t)-y_i(t_0)]}{\Delta t}, \tag{6}$$

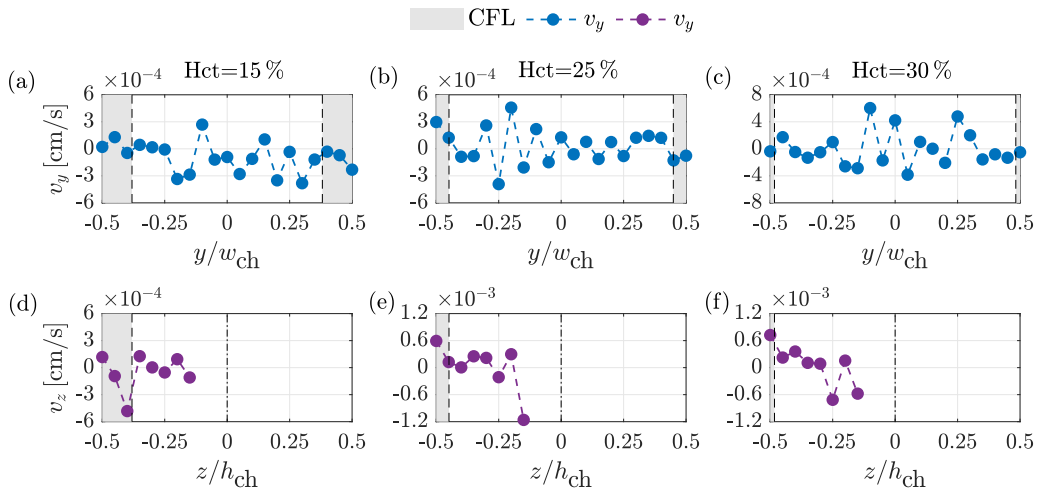

FIG. 7. Distribution of the drift velocity profile of the platelet-size particles at Hct = 15, 25, 30 %. (a)–(c) Spanwise direction y. (d)–(f) Vertical direction z ($-0.5 < z/h_{ch} < -0.15$). The CFL is represented by the gray-shaded area (■).

where y represents the particle coordinate (also valid for z), t_0 the reference time and Δt the time interval between consecutive image frames (20 ms) and N the number of tracked particles. The quantities were estimated under the same conditions as in Sec. III B 1. Figure 7 shows the drift velocity profile along the spanwise y and vertical z directions for different hematocrit (Hct = 15, 25, 30 %). Please note that the results along the vertical direction were limited to $-0.5 < z/h_{ch} < -0.15$ following our discussion in Sec. II B 1.

The results from Fig. 7 show a noisy drift velocity, without revealing any clear trend. We observe large fluctuations from positive to negative drift velocities inside the RBC-rich region. Such result is in agreement with the observed fluctuations in the particle trajectories from Fig. 5 and also with the high-level of particle diffusivity from Fig. 6. It is worth to highlight that such noisy drift velocity arises due to the particle dynamics inside the RBC-suspension flows and not from the measurements, hence it is a description of the ongoing physical phenomena associated with the particle dynamics. The inconclusive drift velocity opposes, however, previous numerical simulations where a lateral drift was reported as in Závodszky *et al.* [21]. Since in our experiments not every particle marginated within our FOV, as already shown in Fig. 6, it becomes difficult to expect a trend in the drift velocity. As we will discuss in Sec. III C, the margination phenomenon in our experiments is not a continuous process and this will therefore have implications in a determination of a lateral drift of the platelet-size particles. Comparing the spanwise y and vertical z directions, we observe a slightly different magnitude. As discussed in the previous Sec. II B 1, it arises from the degradation of the particle detection and does not arise from a physical phenomenon.

3. Particle concentration distribution

The particle concentration ϕ_P was obtained by dividing the spanwise y and vertical z directions into equally spaced bins with a width of 2.5 microns, approximately equal to the particle diameter. The particle count ϕ_P was estimated by counting the particles in each individual bin and normalizing it according to the total number of measured particles. Here again, the values are averaged in space along the mean flow direction x. Following the work of Carboni *et al.* [27], we additionally considered the velocity-weighted particle concentration (ϕ_{Pw}), where the particle concentrations are weighted based on ratio between the maximum velocity and the velocity of the particles. Figure 8 shows the particle concentration distribution, ϕ_P and ϕ_{Pw}, across the spanwise y and vertical z

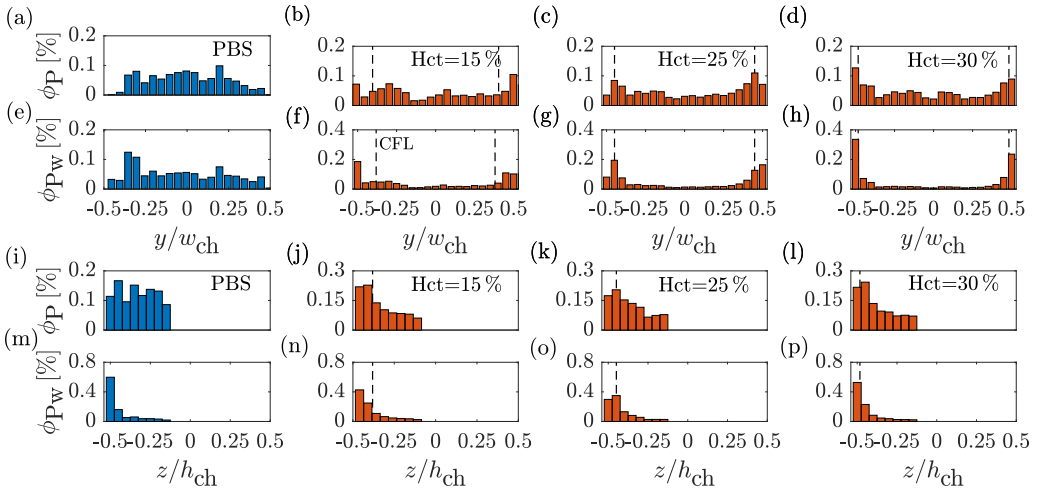

FIG. 8. Time-averaged ϕ_P and velocity-weighted ϕ_{Pw} particle platelet-size particles concentration distribution along the spanwise y and vertical z directions at different hematocrit ($-0.5 < z/h_{ch} < -0.15$). PBS solution (first column). Hct = 15 % (second column). Hct = 25 % (third column). Hct = 30 % (fourth column). δ_{CFL} represents the thickness of the CFL.

directions for different hematocrit (Hct = 15, 25, 30 %). To aid comparisons, the concentration distribution, ϕ_P and ϕ_{Pw}, is also shown for the measurement of a PBS solution, i.e., in the absence of RBCs. Besides, the shape of the particle concentration distribution is similar for the remaining hematocrit.

In the absence of RBCs (i.e., PBS solution), the particles tend to accumulate in the middlemost region of the microchannel, as observed in the experiments of Carboni *et al.* [27] and also in the numerical simulations of Chang *et al.* [15]. As we introduce the RBCs, the interplay between the particles and RBCs leads to the particle margination, and a larger particle accumulation is found in the region close to the wall of the microchannel, for both spanwise y and vertical z directions, see Fig. 8. This distributions are well in agreement with previous works [15,19,21,27].

C. Particle margination

In the previous Sec. III B, we looked into the global particle dynamics through the analysis of the particle diffusivity, drift velocity as well as particle concentration distribution. The latter shows indeed a larger particle concentration near the wall, consistent with the phenomenon of margination. However, as yet, we did not observe any indicators of the margination mechanism, such as for instance a lateral movement of particles toward the wall, as determined by the numerical simulations of Závodszky *et al.* [21].

To shed light into the mechanisms that lead to particle margination, we considered sample particle trajectories of particles flowing close to the CFL. A close-up view over the sample particle trajectories is given in Fig. 9. The selected particle trajectories were obtained at Hct = 30 %. In addition, we highlighted the regions where the particles exhibited the well-known phenomenon of margination: I ( ). Please note that the considered trajectories are limited to the in-plane direction (y), where the RBC-induced masking has no impact as discussed in Sec. II B 1, thus allowing to extract conclusions and provide insights into the mechanisms for particle margination without the influence of the increased uncertainty in z.

Generally, the particle trajectories in Fig. 9 show large trajectory fluctuations and there is no trend when comes to consider a possible lateral drift. Furthermore, our results show that in the same way that a particle migrates toward the wall of the microchannel, it can migrate toward the center

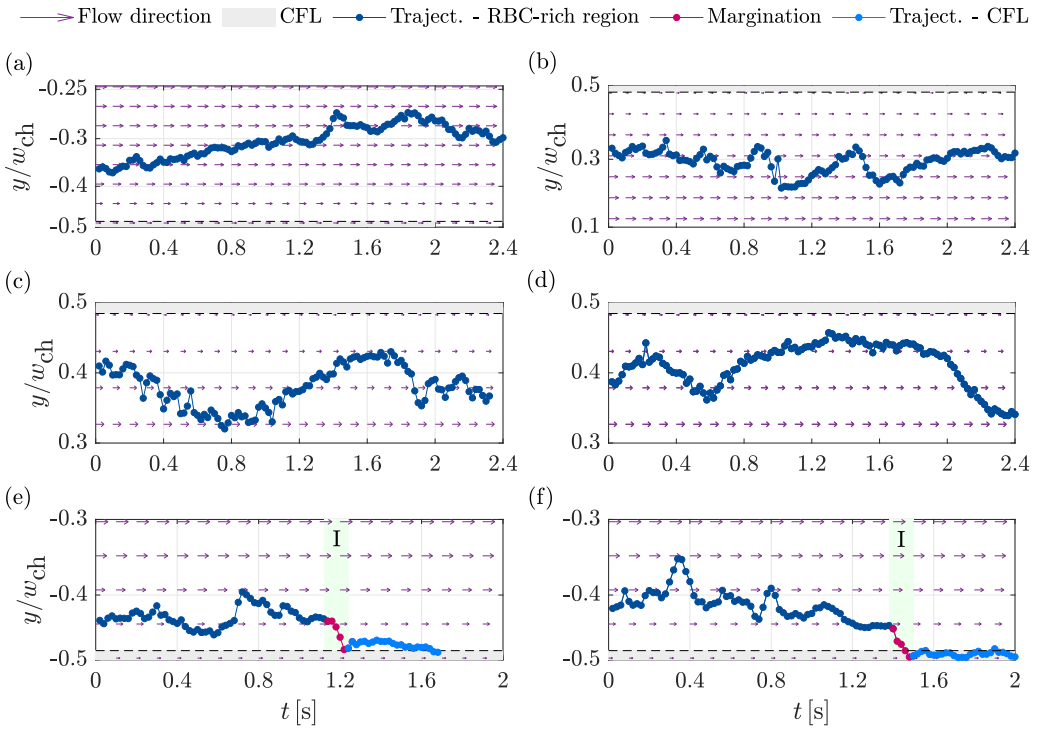

FIG. 9. (a)–(e) Close-up view on sample trajectories of particles flowing inside the RBC-rich region and close to the CFL (Hct = 30 %), including the margination phenomenon: I ( ). The flow direction is represented by the arrows (→) and the CFL is represented by the gray-shaded area ( ).

of the microchannel, i.e., toward the core of the RBC-rich region. The latter is particularly visible in Fig. 9(a), whereas in Figs. 9(b)–9(d) the trajectories exhibit an oscillating-like pattern with both outward and inward migration. As we discussed in Sec. III B, since no external forces are acting on the flow, these changes in the lateral migration can only arise due to the collisions with the RBCs. In other words, the particles will travel laterally depending on the RBCs that may appear on their path, in which every collision event between a particle and the RBCs will result in a variation of the particle trajectory. Such a behavior can thus explain the lack of an overall particle lateral drift from the center of the microchannel toward the wall (see Fig. 7).

Concerning the particle margination, Figs. 9(e) and 9(f) shows sample trajectories of particles flowing inside the RBC-rich region which experienced margination. As in Figs. 9(b)–9(d), we can first observe the same oscillating trajectory, and only in a second instance the particle marginates (I ( )), which is here given by a sudden drop toward the CFL. This sudden drop is often termed as "waterfall phenomenon," and it was already reported by previous numerical simulations [15,18].

Comparing the different trajectories, the primary difference is that in-between those continuous, random collisions with the RBCs and during such paths some particles are presented with an opportunity to marginate, whereas the others suffer additional collisions which prevents them to reach the CFL. As for the former, the margination event is most likely due to a gap between the RBCs flowing at the boundary with the CFL. Such conclusion derives from the fact that during margination the particles exhibited a sudden lateral movement to the CFL i.e, a fast and discontinuous transition, and not a continuous lateral motion from the RBC-rich region toward the CFL. This is in agreement with the numerical simulations of Vahidkhah *et al.* [18], where it was reported that the platelets would take advantage from the cavities between RBCs clusters to marginate. Following this discussion, the present results suggest that the particle margination can

be an unpredictable and discontinuous process, which can be term as an opportunity-based event: Even though the particles are flowing close to the CFL, the margination phenomenon will depend on the RBCs that the particles may find when traveling laterally.

IV. DISCUSSION

The present study enabled to look into the overall particle dynamics and distribution in RBC-suspension flows. We were able to compute relevant quantities such as particle diffusivity (Sec. III B 1), drift velocity (Sec. III B 2) as well as particle concentration distribution (Sec. III B 3). The results point the RBCs as the primary dictator in the particle dynamics. If we consider the high-level of particle diffusivity inside the RBC-rich region, the lower values determined when approaching the CFL (Fig. 6), and that our experimental conditions did not involve any external forces, such results derive from the continuous, random collisions of the particles with the RBCs. As discussed in Sec. III B, in collisions between stiff and floppy particles, the stiffer particle undergoes a larger displacement [22,34]. Moreover, the regions of high and low diffusivity correlate with the expected distribution of the RBCs in the this type of flows. It is well-documented that the RBC concentration is larger around the center of the microchannel, has a steep decrease once approaching the wall, and the CFL is characterized by the absence of RBCs [17,18,21]. Another supporting argument is the particle diffusivity in the absence of RBCs (i.e., for the PBS solution), which has a rather uniform profile and is an order of magnitude lower.

Regarding the near-wall accumulation, we observed that the larger particle concentration is indeed found within the regions close to the wall, which is well-in agreement with previous experimental [27] and numerical [17,21] studies. As for the mechanism for the near-wall accumulation: If the particles experience the well-known phenomenon of margination and migrate toward the wall (i.e., toward the CFL), where there are no collisions with the RBCs, as shown by the low particle diffusivity, the particles do not have an ejecting mechanism from the CFL toward the RBC-rich region as reported by Mehrabadi *et al.* [19]. Therefore, it results in a near-wall particle accumulation and it supports the fact that the particle margination is an irreversible process.

As for the margination mechanism, we did not determine a lateral particle drift toward the wall as in previous studies [17,21]; see Sec. III B 2. Our results instead suggest that the particle lateral motion is a result of continuous, random collisions with the RBCs: It is dictated by the RBCs that may appear during the particle lateral migration. As we observed in Fig. 9, particles flowing close to the CFL can exhibit both inward and outward migration. The trajectories of marginating particles exhibited similar behavior up to the point where the particle was presented with an opportunity to marginate, through a sudden drop. These results point the particle margination as an unpredictable, discontinuous process and more importantly it was an opportunity-based event. Nonetheless, our results were obtained for a fully developed flow and in physical conditions where the flow is at the developing stage, for instance after a bifurcation section, the particle margination may be a result of a continuous lateral drift. Accordingly, at this stage of investigation, it is premature to assume that the particle margination is limited to the sudden drop i.e., the "waterfall phenomenon," observed in our experiments.

V. STUDY LIMITATIONS

First, the washed RBCs lack of bovine serum albumin and other proteins naturally present in blood plasma. However, this is a necessary simplification since unwashed blood is known to cause a high particle adhesion and in such conditions it becomes almost impossible to track the platelet-size particles [27]. We have also taken into account that washed bovine RBCs suspended in PBS provide RBCs with elasticity similar to human RBCs [27,63]. In addition, we used microspheres to mimic platelets, which despite having a similar size to those of platelets, they differ in shape since platelets are known to be spheroidal objects [15,18].

Concerning the measurement method, we have found that GDPT is able to track the platelet-size particle in RBC suspensions flows, however the presence of RBCs makes the particle detection more difficult. As a consequence, we observed a degradation of the particle detection as function of the depth coordinate, which then limited our results to the lower half of the microchannel ($-0.5 < z/h_{ch} < -0.15$). Such a limitation yet does not influence the determination of in-plane coordinates (x and y). Regarding the CFL visualization, we assumed through the symmetry of the microchannel cross-section that the CFL determined for the y axis was also valid for the z axis. If the initial mixing of the RBCs solutions is not sufficient to avoid RBCs sedimentation effect along the microchannel, we may obtain an asymmetric RBCs profile along the z direction. Nonetheless, our recordings were always performed after the same elapsed time since the flow rate was imposed and lasted 50 s (2500 frames at 50 Hz) which ensured consistency and reproducibility of our measurements. However, in future works, the constraint on the GDPT method due to the RBC-induced masking and possible sedimentation must be considered.

VI. CONCLUSIONS

The present experimental study represents the first *in vitro* 3D characterization of platelet-size particles dynamics in RBC-suspension flows, which up to now was limited to numerical simulations. By using the GDPT method, we determined 3D particle trajectories which enabled to look into the mechanisms that contribute for the near-wall accumulation and particle margination in RBC-suspension flows.

The overall picture points to the RBCs as the dictator of the particle dynamics, and therefore the cause for the near-wall particle accumulation and margination, which is well in agreement with previous numerical simulations. Our results suggest that margination is an irreversible, fast, unpredictable and discontinuous process, and more importantly an opportunity-based event. Future work will aim at mimic more relevant biological scenarios, since in most biological systems the fluid transportation is performed in complex networks which feature bifurcations or even contractions-expansions.

ACKNOWLEDGMENTS

Gonçalo Coutinho acknowledges the Ph.D. Scholarship No. 2021.04780.BD attributed by Fundação para a Ciência e Tecnologia (FCT). Massimiliano Rossi acknowledges the financial support by the VILLUM foundation under the Grant No. 00036098. Gonçalo Coutinho, Ana Moita a António Moreira acknowledge Fundação para a Ciência e a Tecnologia (FCT) for partially financing the research trough Project No. PTDC/EME-TED/7801/2020.

[1] S. S. Smyth, R. P. Mcever, A. S. Weyrich, C. N. Morrell, M. R. Hoffman, G. M. Arepally, P. A. French, H. L. Dauerman, and R. C. Becker, Platelet functions beyond hemostasis, J. Thromb. Haemostasis **7**, 1759 (2009).

[2] M. Flamm and S. Diamond, Multiscale systems biology and physics of thrombosis under flow, Ann. Biomed. Eng. **40**, 2355 (2012).

[3] H. L. Goldsmith, G. R. Cokelet, and P. Gaehtgens, Robin fahraeus: Evolution of his concepts in cardiovascular physiology, Am. J. Physiol. **257**, H1005 (1989).

[4] G. Cokelet and H. Goldsmith, Decreased hydrodynamic resistance in the two-phase flow of blood through small vertical tubes at low flow rates, Circ. Res. **68**, 1 (1991).

[5] R. Fåhræus and T. Lindqvist, Viscosity of blood in narrow capillary tubes, Am. J. Physiol. **96**, 562 (1931).

[6] D. Fedosov, B. Caswell, A. Popel, and G. Karniadakis, Blood flow and cell-free layer in microvessels, Microcirculation **17**, 615 (2010).

[7] H. Goldsmith, D. Bell, S. Braovac, A. Steinberg, and F. Mcintosh, Physical and chemical effects of red cells in the shear-induced aggregation of human platelets, Biophys. J. **69**, 1584 (1995).
[8] A. Tilles and E. Eckstein, The near-wall excess of platelet-sized particles in blood flow: Its dependence on hematocrit and wall shear rate, Microvasc. Res. **33**, 211 (1987).
[9] W. S. Uijttewaal, E.-J. Nijhof, P. J. Bronkhorst, E. Den Hartog, and R. M. Heethaar, Near-wall excess of platelets induced by lateral migration of erythrocytes in flowing blood, Am. J. Physiol. **264**, H1239 (1993).
[10] P. Decuzzi, S. Lee, B. Bhushan, and M. Ferrari, A theoretical model for the margination of particles within blood vessels, Ann. Biomed. Eng. **33**, 179 (2005).
[11] K. Müller, D. Fedosov, and G. Gompper, Margination of micro- and nano-particles in blood flow and its effect on drug delivery, Sci. Rep. **4**, 4871 (2014).
[12] F. Glenister, R. Coppel, A. Cowman, N. Mohandas, and B. Cooke, Contribution of parasite proteins to altered mechanical properties of malaria-infected red blood cells, Blood **99**, 1060 (2002).
[13] Y. Zhang, C. Huang, S. Kim, M. Golkaram, M. Dixon, L. Tilley, J. Li, S. Zhang, and S. Suresh, Multiple stiffening effects of nanoscale knobs on human red blood cells infected with plasmodium falciparum malaria parasite, Proc. Natl. Acad. Sci. USA **112**, 6068 (2015).
[14] H.-Y. Chang, X. Li, and G. Karniadakis, Modeling of biomechanics and biorheology of red blood cells in type-2 diabetes mellitus, Biophys. J. **113**, 481 (2017).
[15] H.-Y. Chang, A. Yazdani, X. Li, K. Douglas, C. Mantzoros, and G. Karniadakis, Quantifying platelet margination in diabetic blood flow, Biophys. J., **1**15, 1371 (2018).
[16] G. W. Schmid-Schönbein, S. Usami, R. Skalak, and S. Chien, The interaction of leukocytes and erythrocytes in capillary and postcapillary vessels, Microvasc. Res. **19**, 45 (1980).
[17] L. Crowl and A. Fogelson, Analysis of mechanisms for platelet near-wall excess under arterial blood flow conditions, J. Fluid Mech. **676**, 348 (2011).
[18] K. Vahidkhah, S. L. Diamond, and P. Bagchi, Platelet dynamics in three-dimensional simulation of whole blood, Biophys. J. **106**, 2529 (2014).
[19] M. Mehrabadi, D. Ku, and C. Aidun, A continuum model for platelet transport in flowing blood based on direct numerical simulations of cellular blood flow, Ann. Biomed. Eng. **43**, 1410 (2015).
[20] Q. M. Qi and E. S. G. Shaqfeh, Theory to predict particle migration and margination in the pressure-driven channel flow of blood, Phys. Rev. Fluids **2**, 093102 (2017).
[21] G. Závodszky, B. van Rooij, B. Czaja, V. Azizi, D. Kanter, and A. Hoekstra, Red blood cell and platelet diffusivity and margination in the presence of cross-stream gradients in blood flows, Phys. Fluids **31**, 031903 (2019).
[22] A. Kumar and M. D. Graham, Mechanism of margination in confined flows of blood and other multicomponent suspensions, Phys. Rev. Lett. **109**, 108102 (2012).
[23] M. Mehrabadi, D. N. Ku, and C. K. Aidun, Effects of shear rate, confinement, and particle parameters on margination in blood flow, Phys. Rev. E **93**, 023109 (2016).
[24] C. Bächer, L. Schrack, and S. Gekle, Clustering of microscopic particles in constricted blood flow, Phys. Rev. Fluids **2**, 013102 (2017).
[25] S. Fitzgibbon, A. Spann, Q. Qi, and E. G. Shaqfeh, *In vitro* measurement of particle margination in the microchannel flow: Effect of varying hematocrit, Biophys. J. **108**, 2601 (2015).
[26] R. D'Apolito, G. Tomaiuolo, F. Taraballi, S. Minardi, D. Kirui, X. Liu, A. Cevenini, R. Palomba, M. Ferrari, F. Salvatore, E. Tasciotti, and S. Guido, Red blood cells affect the margination of microparticles in synthetic microcapillaries and intravital microcirculation as a function of their size and shape, J. Control. Rel. **217**, 263 (2015).
[27] E. Carboni, B. Bognet, G. M. Bouchillon, A. L. Kadilak, L. Shor, M. D. Ward, and A. Ma, Direct tracking of particles and quantification of margination in blood flow, Biophys. J. **111**, 1487 (2016).
[28] E. Carboni, B. Bognet, D. Cowles, and A. Ma, The margination of particles in areas of constricted blood flow, Biophys. J. **114**, 2221 (2018).
[29] K. Tatsumi, S. Noguchi, A. Tatsumi, R. Kuriyama, and K. Nakabe, Particle and rigidized red blood cell concentration distributions in microchannel flows, Phys. Fluids **31**, 082006 (2019).

[30] A. Passos, J. Sherwood, E. Kaliviotis, R. Agrawal, C. Pavesio, and S. Balabani, The effect of deformability on the microscale flow behavior of red blood cell suspensions, Phys. Fluids **31**, 091903 (2019).
[31] H. Goldsmith, Red cell motions and wall interactions in tube flow, Fed. Proc. **30**, 1578 (1971).
[32] X. Grandchamp, G. Coupier, A. Srivastav, C. Minetti, and T. Podgorski, Lift and down-gradient shear-induced diffusion in red blood cell suspensions, Phys. Rev. Lett. **110**, 108101 (2013).
[33] S. Losserand, G. Coupier, and T. Podgorski, Migration velocity of red blood cells in microchannels, Microvasc. Res. **124**, 30 (2019).
[34] A. Kumar and M. D. Graham, Segregation by membrane rigidity in flowing binary suspensions of elastic capsules, Phys. Rev. E **84**, 066316 (2011).
[35] E. Eckstein, A. Tilles, and F. Millero III, Conditions for the occurrence of large near-wall excesses of small particles during blood flow, Microvasc. Res. **36**, 31 (1988).
[36] R. Barnkob, C. J. Kähler, and M. Rossi, General defocusing particle tracking, Lab Chip **15**, 3556 (2015).
[37] R. Barnkob and M. Rossi, General defocusing particle tracking: Fundamentals and uncertainty assessment, Exp. Fluids **61**, 110 (2020).
[38] M. Rossi and R. Barnkob, A fast and robust algorithm for general defocusing particle tracking, Meas. Sci. Technol. **32**, 014001 (2020).
[39] J. Barbee and G. Cokelet, The fahraeus effect, Microvasc. Res. **3**, 6 (1971).
[40] Y. Son, Determination of shear viscosity and shear rate from pressure drop and flow rate relationship in a rectangular channel, Polymer **48**, 632 (2007).
[41] R. Barnkob and M. Rossi, Defocustracker: A modular toolbox for defocusing-based, single-camera, 3D particle tracking, J. Open Res. Software **9**, 22 (2021).
[42] J. Lewis, Fast template matching, Vision Interface **95**, 120 (1994).
[43] N. Malik, T. Dracos, and D. Papantoniou, Particle tracking velocimetry in three-dimensional flows—Part II: Particle tracking, Exp. Fluids **15**, 279 (1993).
[44] https://gitlab.com/defocustracking.
[45] C. Cierpka, M. Rossi, R. Segura, and C. J. Kähler, On the calibration of astigmatism particle tracking velocimetry for microflows, Meas. Sci. Technol. **22**, 015401 (2011).
[46] G. Coutinho, M. Rossi, A. Moita, and A. Moreira, 3D particle tracking velocimetry applied to platelet-size particles in red blood cells suspensions flows through square microchannels, in *Proceedings of the 20th International Symposium on Applications of Laser and Imaging Techniques to Fluid Mechanics*, Conference Series (Lisbon, Portugal, 2021), pp. 233–244.
[47] G. Coutinho, A. Moita, A. Ribeiro, A. Moreira, and M. Rossi, On the characterization of bias errors in defocusing-based 3D particle tracking velocimetry for microfluidics, Exp. Fluids **64**, 106 (2023).
[48] G. Cokelet, Poiseuille award lecture. viscometric, *in vitro* and *in vivo* blood viscosity relationships: How are they related? Biorheology **36**, 343 (1999).
[49] P. Bagchi, Mesoscale simulation of blood flow in small vessels, Biophys. J. **92**, 1858 (2007).
[50] K. Yeo and M. Maxey, Numerical simulations of concentrated suspensions of monodisperse particles in a Poiseuille flow, J. Fluid Mech. **682**, 491 (2011).
[51] H. Bruus, *Theoretical Microfluidics* (Oxford University Press, Oxford, UK, 2008).
[52] A. R. Pries, D. Neuhaus, and P. Gaehtgens, Blood viscosity in tube flow: Dependence on diameter and hematocrit, Am. J. Physiol.: Heart Circ. Physiol. **263**, H1770 (1992).
[53] L. E. Bayliss, The rheology of blood and lymph, in *Deformation and Flow in Biological Systems*, edited by A. Frey-Wyssling (North Holland Pub. Co., Amsterdam, 1952),pp. 355–418.
[54] R. Lima, S. Wada, S. Tanaka, M. Takeda, T. Ishikawa, K.-i. Tsubota, Y. Imai, and T. Yamaguchi, *In vitro* blood flow in a rectangular pdms microchannel: Experimental observations using a confocal micro-piv system, Biomed. Microdevices **10**, 153 (2008).
[55] S. Roman, S. Lorthois, P. Duru, and F. Risso, Velocimetry of red blood cells in microvessels by the dual-slit method: Effect of velocity gradients, Microvasc. Res. **84**, 249 (2012).
[56] S. Whittaker and F. Winton, The apparent viscosity of blood flowing in the isolated hindlimb of the dog, and its variation with corpuscular concentration, J. Physiol. **78**, 339 (1933).
[57] D. Fedosov, W. Pan, B. Caswell, G. Gompper, and G. Karniadakis, Predicting human blood viscosity in silico, Proc. Natl. Acad. Sci. USA **108**, 11772 (2011).

[58] D. A. Reasor Jr., M. Mehrabadi, D. Ku, and C. Aidun, Determination of critical parameters in platelet margination, Ann. Biomed. Eng. **41**, 238 (2013).

[59] J. M. Sherwood, D. Holmes, E. Kaliviotis, and S. Balabani, Spatial distributions of red blood cells significantly alter local haemodynamics, PLoS One **9**, e100473 (2014).

[60] C. Alonso, A. Pries, O. Kiesslich, D. Lerche, and P. Gaehtgens, Transient rheological behavior of blood in low-shear tube flow: Velocity profiles and effective viscosity, Am. J. Physiol. **268**, H25 (1995).

[61] H. Goldsmith, The microrheology of red blood cell suspensions, J. Gen. Physiol. **52**, 5 (1968).

[62] V. Turitto, A. Benis, and E. Leonard, Platelet diffusion in flowing blood, Ind. Eng. Chem. Fundam. **11**, 216 (1972).

[63] T. Amin and J. Sirs, The blood rheology of man and various animal species, Q. J. Exp. Physiol. **70**, 37 (1985).